Acta Crystallographica Section B
Structural Science
ISSN 0108-7681

Structures and phase transitions of *B*-Ta_2O_5 and *Z*-Ta_2O_5: two high-pressure forms of Ta_2O_5

I. P. Zibrov,[a] V. P. Filonenko,[b] M. Sundberg[c]* and P.-E. Werner[c]

[a]Institute of Crystallography, Russian Academy of Sciences, 117 333 Moscow, Russia, [b]Institute for High Pressure Physics, Russian Academy of Sciences, Troitsk, 142190 Moscow Region, Russia, and [c]Department of Inorganic and Structural Chemistry, Arrhenius Laboratory, Stockholm University, S-106 91 Stockholm, Sweden

Correspondence e-mail: marsu@inorg.su.se

Received 21 January 2000
Accepted 10 April 2000

A sample of Ta_2O_5, ditantalum pentaoxide, heat-treated in a 'toroid'-type high-pressure chamber at P = 8 GPa and T = 1470 K, was studied by X-ray powder diffraction and high-resolution transmission electron microscopy (HRTEM). Two high-pressure modifications of Ta_2O_5, isostructural with *B*-Nb_2O_5 and *Z*-Nb_2O_5, were identified from the X-ray powder pattern. Both structures were refined by the Rietveld method from the X-ray diffraction data: *B*-Ta_2O_5, a = 12.7853 (4), b = 4.8537 (1), c = 5.5276 (2) Å, β = 104.264 (2)°, V = 332.45 Å^3, Z = 4, space group $C2/c$; *Z*-Ta_2O_5, a = 5.2252 (1), b = 4.6991 (1), c = 5.8534 (1) Å, β = 108.200 (2)°, V = 136.53 Å^3, Z = 2, space group $C2$. The *Z*-Ta_2O_5 modification is new. The Ta atoms are six-coordinated in *B*-Ta_2O_5 and seven-coordinated in *Z*-Ta_2O_5. The two structures are closely related, which makes an intergrowth and a transformation between them possible. An idealized model of the intergrowth structure has been given. The HRTEM study showed defect-rich *B*-Ta_2O_5 crystals, which could be interpreted as an intergrowth between the *B*-Ta_2O_5 and *Z*-Ta_2O_5 phases.

1. Introduction

It is well known that ditantalum pentaoxide undergoes a phase transformation from the low-temperature form, *L*-Ta_2O_5 (β phase), to the high-temperature polymorph, *H*-Ta_2O_5 (α phase) at ~1630 K (Lagergren & Magnéli, 1952). In both structures the Ta atoms are six- and seven-coordinated in the form of TaO_6 octahedra and pentagonal TaO_7 bipyramids (Stephenson & Roth, 1971*a*,*b*).

The ε-Ta_2O_5 modification was reported by Izumi & Kodama (1979) to form from tantalic acid treated with hydrochloric acid under the hydrothermal conditions P = 20 MPa and T = 570–620 K. This phase, which is isomorphous with *B*-Nb_2O_5, contains six-coordinated Ta atoms (TaO_6 octahedra) only. We prefer to use the designation *B*-Ta_2O_5 for this phase to emphasize the structural analogy with *B*-Nb_2O_5. Two additional polymorphs, *TT*-Ta_2O_5 and *T*-Ta_2O_5, have been prepared by soft chemistry methods (Hummel *et al.*, 1992). The latter structure is built from TaO_6 octahedra and pentagonal TaO_7 bipyramids. Several metastable modifications of Ta_2O_5 have also been reported over the years and a table showing the stable and metastable polymorphs of Ta_2O_5 is given in the paper by Hummel *et al.* (1992).

The present work was undertaken to investigate which modifications of Ta_2O_5 are formed at P = 8.0 GPa by using the high-pressure synthesis method developed for the tungsten–oxygen and niobium–oxygen systems (Zibrov *et al.*, 1998).

2. Experimental

A Ta_2O_5 powder of 99.9% purity was pressed into pellets 4 mm in height and 5 mm in diameter. The pellets were covered with Mo or Pt foils to prevent contact between the specimen and the surrounding high-pressure cell material. A detailed description of the equipment and the experimental procedure has been given elsewhere (Zibrov *et al.*, 1998). The high-pressure synthesis was performed at $P = 8.0$ GPa and $T = 1470$ K. The temperature was held for 5 min, followed by quenching the sample to room temperature at a rate of $\sim$100 K s^{-1} before the pressure was released.

The sample was then analyzed by X-ray powder diffraction and high-resolution transmission electron microscopy (HRTEM). The TEM samples were prepared by crushing a small quantity of the material under *n*-butanol in an agate mortar. A few drops of the resulting suspension were placed onto a porous carbon film supported by a copper grid. The HRTEM study was performed in a Jeol 3010 microscope (double tilt $\pm$ 20°, side-entry goniometer stage) operating at 300 kV. Simulated images were calculated using a local PC version of the *SHRLI* suite of multislice programs (O'Keefe *et al.*, 1978). The purity of the sample was checked by energy-dispersive X-ray spectroscopy (EDS analysis), using a Jeol 2000FXII transmission electron microscope equipped with a LINK AN10000 X-ray microanalysis system. The structure models are produced with *ATOMS* by Shape Software.

3. X-ray diffraction studies

For preliminary studies, an X-ray diffraction photograph was recorded in a subtraction geometry Guinier–Hägg focusing camera, with strictly monochromated Cu $K\alpha_1$ radiation (λ = 1.540598 Å). Finely powdered silicon (a = 5.430940 Å at 298 K; standard reference material 640b from the National Bureau of Standards) was added as an internal 2θ standard. The photograph was measured with an automatic single-beam microdensitometer (Johansson *et al.*, 1980). The positions of the silicon peaks were used to correct for sample displacement, zero-point error and film shrinkage. The X-ray pattern was found to correspond to a mixture of two phases which are isostructural with *B*- and *Z*-Nb_2O_5 (Zibrov *et al.*, 1998). Their unit-cell parameters were very slightly different from those of the Nb-containing phases.

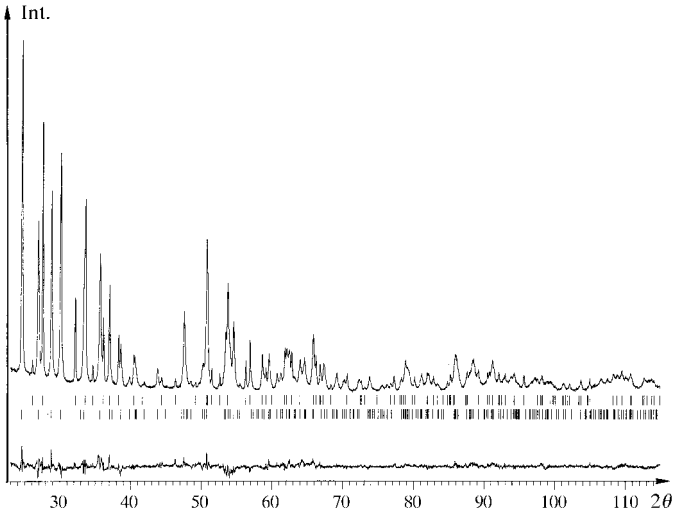

Figure 1
X-ray Rietveld refinement of *B*-Ta_2O_5 + *Z*-Ta_2O_5. The upper curve illustrates the observed data, and the lower curve the difference between observed and calculated data. The positions of all the allowed Bragg reflections are indicated by rows of vertical tick marks: *Z*-Ta_2O_5 upper and *B*-Ta_2O_5 lower marks.

Table 1
Experimental details.

	B-Ta_2O_5	*Z*-Ta_2O_5
Crystal data		
Chemical formula	Ta_2O_5	Ta_2O_5
Chemical formula weight	441.89	441.89
Cell setting	Monoclinic	Monoclinic
Space group	*C*2/*c*	*C*2
a (Å)	12.7853 (4)	5.2252 (1)
b (Å)	4.8537 (1)	4.6991 (1)
c (Å)	5.5276 (2)	5.8534 (1)
β (°)	104.264 (2)	108.200 (2)
V (Å^3)	332.45	136.53
Z	4	2
D_x (Mg m^{-3})	8.83	10.75
Radiation type	Cu $K\alpha_1$	Cu $K\alpha_1$
Wavelength (Å)	1.54056	1.54056
Temperature (K)	293	293
Data collection		
Diffractometer	Stoe PSD	Stoe Small PSD
Refinement		
Refinement on	I_{net}	I_{net}
$FWHM_{min}$ (°)	0.185	0.127
$FWHM_{max}$ (°)	0.707	0.229
R_f	0.026	0.032
R_p	0.054	0.054
R_{wp}	0.071	0.071
d†	0.49	0.49
bl‡	3.06	3.06
No. of parameters used	47	47
Weighting scheme	$1/Y_i$	$1/Y_i$
$(\Delta/\sigma)_{max}$	0.2	0.2
Extinction method	None	None
Source of atomic scattering factors	*International Tables for X-ray Crystallography* (1974, Vol. IV)	*International Tables for X-ray Crystallography* (1974, Vol. IV)
Computer programs		
Data collection	Stoe Stadi/P, Powdat	Stoe Stadi/P, Powdat
Cell refinement	*DBW*3.2S (Wiles *et al.*, 1988)	*DBW*3.2S (Wiles *et al.* 1988)
Data reduction	Stoe Stadi/P, Rawdat	Stoe Stadi/P, Rawdat
Structure refinement	*DBW*3.2*S* (Wiles *et al.*, 1988)	*DBW*3.2*S* (Wiles *et al.*, 1988)

† *d* = Durbin–Watson statistic *d* value according to Hill & Flack (1987). ‡ *bl* = Correction factor for serial correlation, calculated by the method of Bérar & Lelann (1991).

Diffraction data for structure refinements were collected on a Stoe Stadi/P powder diffractometer with a rotating sample in the symmetric transmission mode. A symmetric focusing germanium monochromator (focal distance = 440 mm) was used to give pure Cu $K\alpha_1$ radiation. The diffraction data were collected with a small linear position-sensitive detector (PSD)

Table 2
Fractional atomic coordinates and equivalent isotropic displacement parameters (Å^2) for *B*-Ta_2O_5.

$$U_{eq} = (1/3)\Sigma_i\Sigma_j U^{ij} a^i a^j \mathbf{a}_i.\mathbf{a}_j.$$

	Site	*x*	*y*	*z*	U_{eq}
Ta	8(*f*)	0.1395 (1)	0.2470 (15)	0.2623 (2)	1.10 (3)
O1	4(*e*)	0	0.102 (4)	1/4	1.8 (2)
O2	8(*f*)	0.389 (2)	0.051 (2)	0.990 (4)	1.8 (2)
O3	8(*f*)	0.299 (1)	0.431 (3)	0.355 (3)	1.8 (2)

Table 3
Fractional atomic coordinates and equivalent isotropic displacement parameters (Å^2) for *Z*-Ta_2O_5.

$$U_{eq} = (1/3)\Sigma_i\Sigma_j U^{ij} a^i a^j \mathbf{a}_i.\mathbf{a}_j.$$

	Site	*x*	*y*	*z*	U_{eq}
Ta	4(*c*)	0.2172 (3)	0	0.2696 (4)	1.73 (6)
O1	4(*c*)	0.189 (4)	0.164 (5)	0.934 (4)	0.7 (3)
O2	4(*c*)	0.090 (5)	0.681 (5)	0.323 (4)	0.7 (3)
O3	2(*b*)	0	0.201 (7)	1/2	0.7 (3)

covering 6.4° in 2θ. The PSD was moved in steps of 0.2°, 200 s per step, thus giving an average intensity of 32 measurements at each 2θ position. It has been found that the angular resolution of the diffractometer operated under these conditions is approximately the same as that of a Guinier–Hägg photograph. The 2θ range measured was $10 < 2\theta < 130°$. The peak shapes were described by a symmetric pseudo-Voigt function. The Rietveld program used was a local version of the program *DBW*3.2*S* (Wiles *et al.*, 1988). Owing to the overlap between peaks from the two phases, only cell parameters from the final Rietveld refinement are reported in Table 1, where also some general parameters from the refinement are shown. The positional parameters obtained for *B*- and *Z*-Ta_2O_5 are given in Tables 2 and 3, respectively. In Fig. 1 the observed diffractometer data and the difference between observed and calculated data are shown.[1]

The final *R* factors obtained from the Rietveld refinements are very small. Thus, for example, the structure factor *R* values for *B*-Ta_2O_5 and *Z*-Ta_2O_5 are 0.026 and 0.032, respectively. In spite of these very small *R* factors, the accuracy in the positional coordinates is rather low, especially for the *Z* phase with a weight fraction of only 0.27, calculated from the refined scale factors. Another reason for the large s.u.'s in the positional coordinates is the severe serial-correlation problems, frequently present in full-profile Rietveld refinement studies, in this case leading to a correction factor of 3.06 (the *bl* factor reported in Table 1). This correction factor is applied in the calculation of s.u.'s for the interatomic distances shown in Tables 4 and 5.

Table 4 shows a comparison between *B*-Ta_2O_5 (this study) and a single-crystal study of *B*-Nb_2O_5 (Ercit, 1991). Although

Table 4
Selected interatomic distances (Å).

Comparison of single-crystal data for *B*-Nb_2O_5 (Ercit, 1991) with data for *B*-Ta_2O_5. The *bl* factor (*cf.* Table 1) is applied on the *B*-Ta_2O_5 data.

B-Ta_2O_5		*B*-Nb_2O_5	
Ta—Ta^{i}	3.351 (5)	Nb—Nb^{i}	3.4042 (6)
Ta—Ta^{ii}	3.536 (6)	Nb—Nb^{ii}	3.5758 (7)
Ta—O1	1.90 (2)	Nb—O1	1.910 (1)
Ta—O2^{iii}	2.10 (5)	Nb—O2^{iii}	2.081 (2)
Ta—O2^{i}	1.67 (6)	Nb—O2^{i}	1.786 (2)
Ta—O3	2.17 (5)	Nb—O3	2.114 (2)
Ta—O3^{i}	2.24 (5)	Nb—O3^{i}	2.204 (2)
Ta—O3^{iv}	1.91 (5)	Nb—O3^{iv}	1.950 (2)
O1—O1^{v}	2.94 (3)	O1—O1^{v}	2.958 (1)
O1—O2^{vi}	2.80 (6)	O1—O2^{vi}	2.733 (2)
O1—O2^{i}	2.75 (6)	O1—O2^{i}	2.860 (2)
O1—O3^{i}	2.94 (5)	O1—O3^{i}	2.899 (2)
O1—O3^{iv}	2.89 (5)	O1—O3^{iv}	3.001 (3)
O2—O2^{vii}	2.86 (9)	O2—O2^{vii}	2.928 (4)
O2—O2^{viii}	2.81 (9)	O2—O2^{viii}	2.837 (3)
O2—O3^{ix}	2.80 (8)	O2—O3^{ix}	2.636 (4)
O2—O3^{viii}	2.63 (6)	O2—O3^{viii}	2.708 (3)
O2—O3^{i}	2.68 (8)	O2—O3^{i}	2.808 (3)
O2—O3^{x}	2.79 (6)	O2—O3^{x}	2.832 (3)
O3—O3^{i}	2.87 (7)	O3—O3^{i}	2.659 (3)
O3—O3^{x}	2.84 (7)	O3—O3^{x}	2.869 (3)
O3—O3^{iv}	2.84 (6)	O3—O3^{iv}	2.889 (3)

Symmetry codes: (i) $\frac{1}{2}-x, \frac{1}{2}-y, 1-z$; (ii) $-x, y, \frac{1}{2}-z$; (iii) $\frac{1}{2}-x, \frac{1}{2}+y, \frac{3}{2}-z$; (iv) $\frac{1}{2}-x, -\frac{1}{2}+y, \frac{1}{2}-z$; (v) $-x, -y, -z$; (vi) $\frac{1}{2}-x, \frac{1}{2}+y, \frac{3}{2}-z$; (vii) $1-x, -y, 2-z$; (viii) $x, -y, \frac{1}{2}+z$; (ix) $\frac{1}{2}-x, -\frac{1}{2}+y, \frac{3}{2}-z$; (x) $x, 1-y, \frac{1}{2}+z$.

the Me—Me distances are slightly different, it is not easy to identify statistically verifiable differences between the TaO_6 and NbO_6 octahedra. It is even more difficult to find any other differences between interatomic distances in *Z*-Ta_2O_5 and *Z*-Nb_2O_5 (*cf.* Table 5) besides some minor deviations between the Me—Me distances. In general it can be concluded that the type of seven-coordination found in *Z*-Nb_2O_5, with one short and six longer Me—O distances, is also present in *Z*-Ta_2O_5. The crystal structure of *Z*-Ta_2O_5 is shown in Fig. 2. The Ta atoms are coordinated by four O atoms in or near one plane

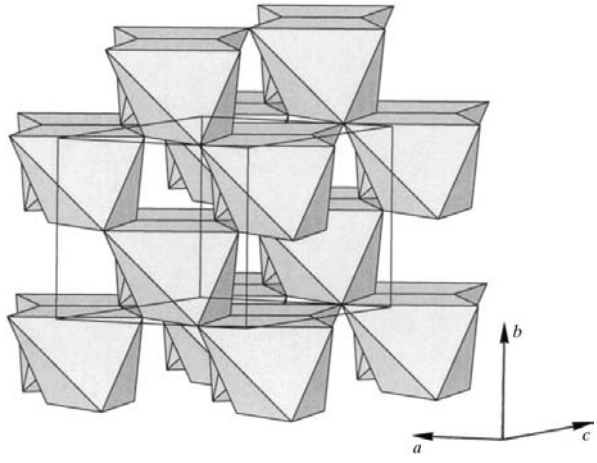

Figure 2
The crystal structure of *Z*-Ta_2O_5. Note the irregular polyhedra of seven-coordinated Ta, which form pairs of edge-sharing polyhedra in two layers at $y = 0$ and $y = 1/2$.

[1] Supplementary data for this paper are available from the IUCr electronic archives (Reference: OS0050). Services for accessing these data are described at the back of the journal.

above and by three O atoms in or near a plane below, giving the irregular coordination of seven O atoms around tantalum (TaO_7 polyhedron).

The very large increase in density, from 8.83 g cm^{-3} in B-Ta_2O_5 to 10.75 g cm^{-3} in Z-Ta_2O_5, is probably the reason for some very short O—O contacts in the Z phase. Thus, the volume per O atom is reduced from 16.6 to 13.6 Å^3. As can be seen in Table 5 similar short O—O contacts were also found in Z-Nb_2O_5 (Zibrov *et al.*, 1998). Although the O2—O3 distance of 2.07 Å in Z-Ta_2O_5 and the O1—O1 distance of 2.03 Å in Z-Nb_2O_5 should be judged in relation to the s.u.'s 0.08 and 0.12 Å, respectively, the existence of O—O contacts around 2.16–2.18 Å in the Ta and Nb Z-phases seems to be statistically verified (*cf.* Table 5). The shortest O—O contact reported by Shannon & Prewitt (1969) is 2.15 Å in the calcite-type structure of $NaNO_3$.

4. Structural relationship

The crystal structures of B-Ta_2O_5 and Z-Ta_2O_5 are closely related, as can be seen from Figs. 3 and 4, respectively. Both phases have unit cells with monoclinic symmetry and the b-axis parameters are approximately the same (~4.8 Å). The small difference, ~0.3 Å, between the length of the B-Ta_2O_5 c axis and the length of the Z-Ta_2O_5 a axis should also be noted.

The B-Ta_2O_5 structure, projected along [010] and [001] in Figs. 3(*a*) and (*b*), respectively, can be described as built up from rutile-like slabs of edge-sharing TaO_6 octahedra, two octahedra wide, and linked by corner-sharing. The O atoms are arranged in a slightly distorted hexagonally close-packed array (h.c.p.). Alternatively, the B-Ta_2O_5 structure can be considered by layers stacked parallel to the *ac* plane, as can be seen in Figs. 3(*c*)–(*f*). The two layers at y = 3/4 and y = 1/4 (Figs. 3*c* and *e*) consist of isolated strings of TaO_6 octahedra along [101]. The strings are composed of pairs of edge-sharing octahedra linked in a zigzag arrangement by corner-sharing.

The Z-Ta_2O_5 structure, shown in [010] and [100] projections in Figs. 4(*a*) and (*b*), is much more dense than the B-Ta_2O_5 structure in Figs. 3(*a*) and (*b*). It can be regarded as built up from 'rutile'-related slabs of edge-sharing TaO_7 polyhedra, two polyhedra wide. The slabs, which are parallel to the a axis, are connected by sharing O-atom corners. In analogy with the B-Ta_2O_5 structure, Z-Ta_2O_5 can be considered as a layer structure, of which the two levels parallel to the *ac* plane at y = 0 and y = 1/2 are shown in Figs. 4(*c*)–(*f*). Fig. 4(*c*) shows that the layer is built up of strings consisting of edge-sharing pairs of TaO_7 polyhedra, linked by corners to form a zigzag array along [101]. In Z-Ta_2O_5 the strings are mutually linked by corner-sharing to form a two-dimensional network of corner-sharing pairs of TaO_7 polyhedra, as can be seen in Figs. 4(*c*) and (*e*). The similarity between the two structures is apparent.

The fact that B-Ta_2O_5 and Z-Ta_2O_5 have closely related structures with b-axis parameters of ~4.8 Å, and that they can be considered as layer structures

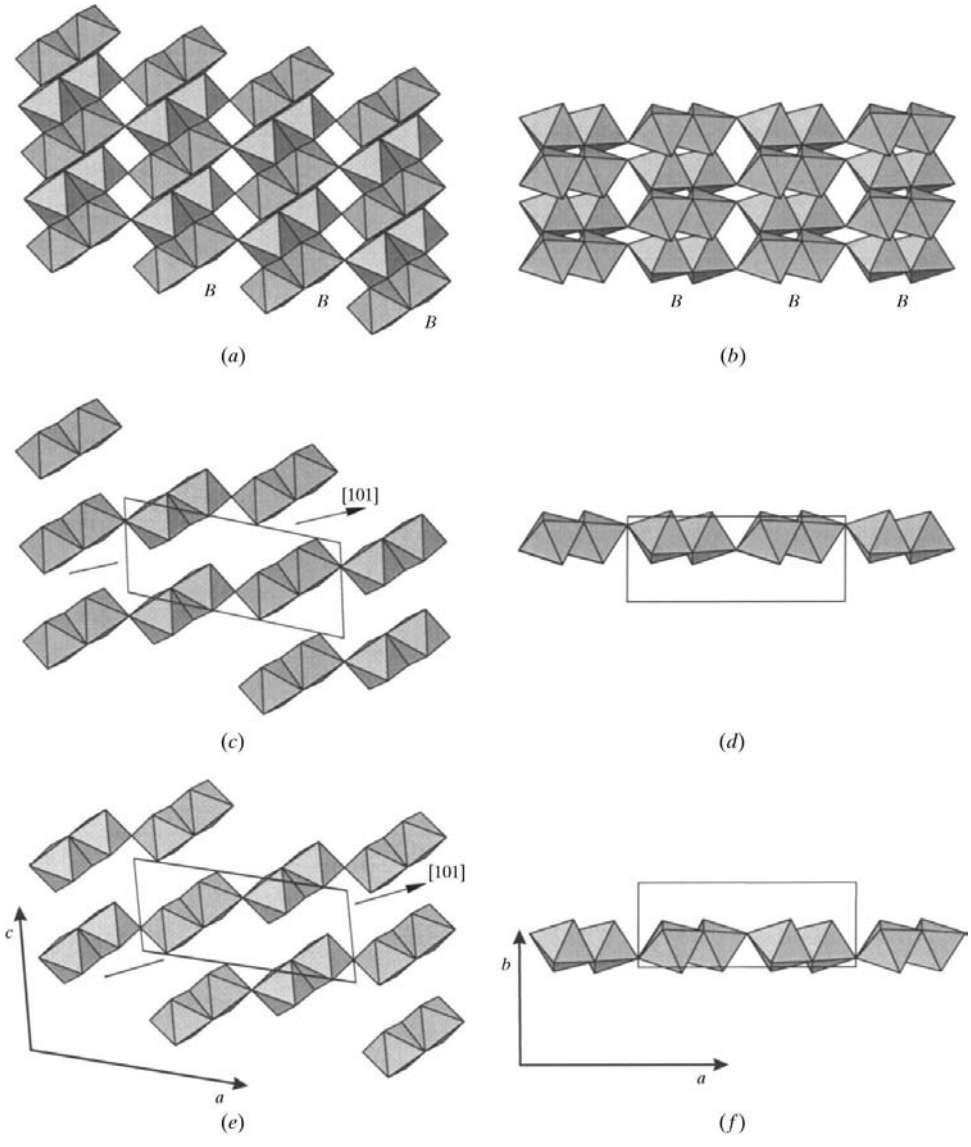

Figure 3
The crystal structure of B-Ta_2O_5 is projected along (*a*) [010] and (*b*) [001]. The two layers of octahedra at y = 3/4 and y = 1/4 are shown in (*c*) and (*e*) ([010] projection), and in (*d*) and (*f*) ([001] projection). The unit cell is drawn.

parallel to the *ac* plane, makes an intergrowth between them very likely. The structures can be mutually linked by sharing O-atom corners through a common oxygen plane (Fig. 5*a*), which is parallel to *bc* in *B*-Ta_2O_5 and *ab* in *Z*-Ta_2O_5. A possible model of the intergrowth boundary is illustrated in Figs. 5(*b*) and (*c*). The model suggests that the two modifications can transform from one form to another by small metal- and oxygen-atom displacements with an accompanying compression of the structures (when pressure is applied) *B*-$Ta_2O_5 \rightarrow$ *Z*-Ta_2O_5, or expansion *Z*-$Ta_2O_5 \rightarrow$ *B*-Ta_2O_5 (when pressure is released).

5. Electron microscopy study

The HRTEM study of thin fragments from the Ta_2O_5 sample revealed many faulted crystals. Two examples of HRTEM micrographs, taken close to Scherzer conditions, of *B*-Ta_2O_5 crystals in [010] and [001] projections are presented in Figs. 6(*a*) and Fig. 7(*a*), respectively. The corresponding electron diffraction patterns are inserted. Both images show well ordered crystal regions on both sides of a defect area. The black spots in Fig. 6(*a*) represent projected metal atoms. The slabs, two black spots wide (marked *B*), correspond to the rutile-like slabs of TaO_6 octahedra in the *B*-Ta_2O_5 structure. The wider slabs, four or six dark spots wide (marked *Z*), indicate either an intergrowth of the *Z*-Ta_2O_5 structure or a transition state between the two modifications.

Theoretical image simulations were performed for the *B*-Ta_2O_5 and *Z*-Ta_2O_5 structures, using the atomic coordinates obtained in the X-ray powder diffraction study (Tables 2 and 3). It was clear from the calculated electron diffraction patterns, the projected potentials and the simulated images that the two structures will give rise to similar HRTEM images at some defocus values. A set of simulated images in [010] projections of *B*-Ta_2O_5 (top) and *Z*-Ta_2O_5 (bottom) is shown in Fig. 6(*b*). The rutile-like slabs of polyhedra in the structures correspond to the slabs, two black spots wide, which can be seen in all simulated images. The black spots are slightly closer together and not so well resolved in the simulated images of the *Z*-Ta_2O_5 structure at the defocus values of −200 and −250 Å. The HRTEM micrograph in Fig. 6(*a*), which illustrates the local structure of a *B*-Ta_2O_5 fragment at the atomic level, clearly shows that the projected Ta atoms (dark spots) in the slabs are not lined up in such straight rows parallel to the *a* axis as the simulated images display. Some spots are closer together and less well resolved, while others are further apart, especially in the wider slabs in the micrograph. These contrasting features indicate either some local compression of the *B*-Ta_2O_5 structure or some microdomains of *Z*-Ta_2O_5 intergrown with the *B*-Ta_2O_5 structure.

The electron diffraction pattern inserted in Fig. 7(*a*) shows that the *B*-Ta_2O_5 structure dominates in this crystal fragment. There is also good agreement between the contrast features in the simulated image of the *B*-Ta_2O_5 structure in the [001] projection (Fig. 7*c*) and the region surrounding the defect area in Fig. 7(*a*), which confirms the structure interpretation. The boundary between the defect area and the *B*-Ta_2O_5 region is disordered. Fig. 7(*b*) shows a simulated image of *Z*-Ta_2O_5 under the same experimental conditions as used in Fig. 7(*c*). There are some apparent similarities between the contrast

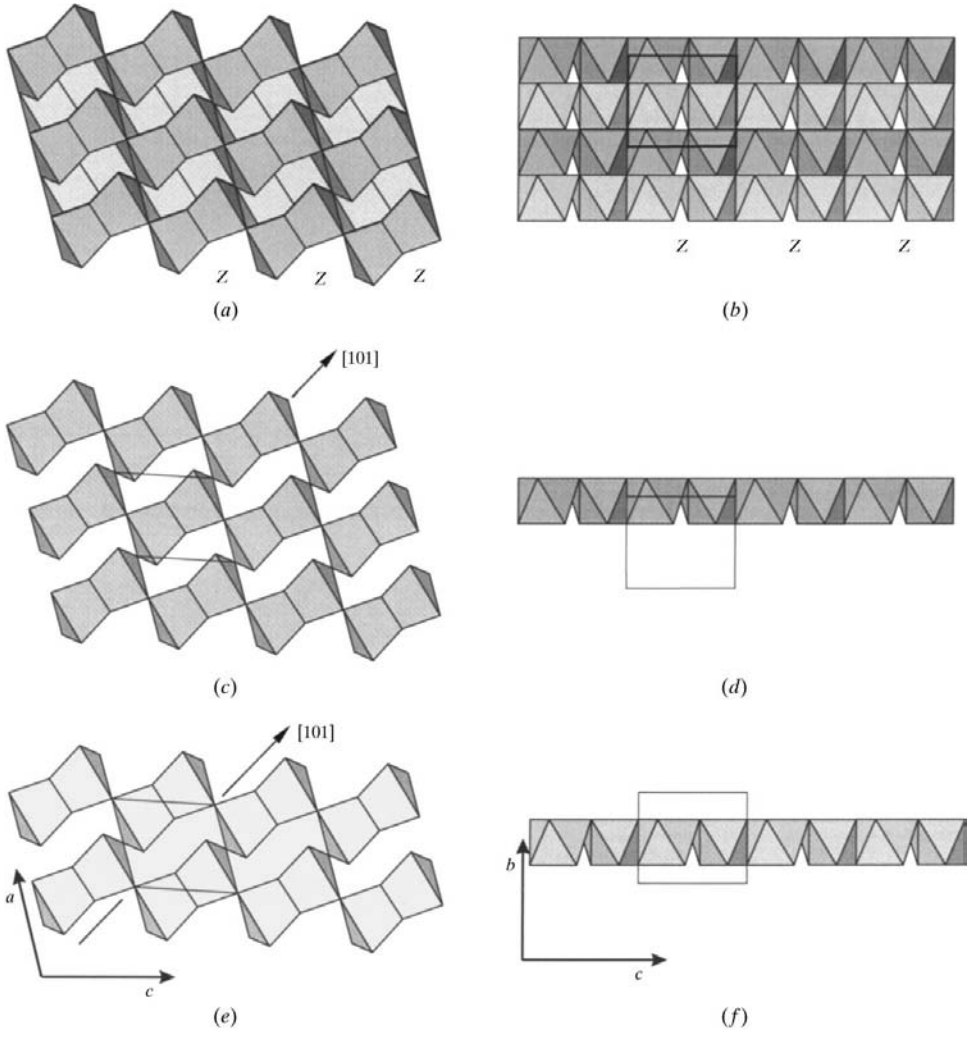

Figure 4
The crystal structure of *Z*-Ta_2O_5 is projected along (*a*) [010] and (*b*) [100]. The two layers of polyhedra at $y = 0$ and $y = 1/2$ are shown in (*c*) and (*e*) ([010] projection) and in (*d*) and (*f*) in [100] projection. The unit cell is outlined. The drawings are produced with *ATOMS* by Shape Software.

features in the defect area and the simulated image in Fig. 7(*b*), which suggests a coexistence of the two modifications. It should be noted, however, that no ordered fragment of *Z*-Ta_2O_5 has been observed so far.

6. Phase transformations

The X-ray and HRTEM results presented above show that the *L*-Ta_2O_5 modification was not stable under the high-pressure conditions $P = 8.0$ GPa and $T = 1470$ K. A two-phase mixture of the *B*-Ta_2O_5 and *Z*-Ta_2O_5 polymorphs was obtained instead. Heating this product in an oxygen atmosphere to $T = 770$ K under ambient pressure resulted in a single-phase sample of *B*-Ta_2O_5. We also noted that further heating of the product under ambient pressure conditions resulted in transformation from *B*-Ta_2O_5 to *L*-Ta_2O_5, starting slightly above $T = 1070$ K. The latter phase transformation has been reported by Izumi & Kodama (1979). All products were white with a very faint touch of grey, suggesting that the phases are fully oxidized and thus of Ta_2O_5 stoichiometry. Moreover, no impurity peaks were observed in the EDS spectra. All these results suggest that upon heating under pressure *L*-Ta_2O_5 undergoes a phase transformation to *B*-Ta_2O_5, which is transformed to *Z*-Ta_2O_5 by increasing the pressure. The latter modification is probably not completely stable and partly

Table 5
Selected interatomic distances (Å).

Comparison of *Z*-Nb_2O_5 data from Zibrov *et al.* (1998) and *Z*-Ta_2O_5. The s.u.'s are calculated with *bl* factors (*cf.* Table 1) applied.

Z-Ta_2O_5		*Z*-Nb_2O_5	
Ta—Ta^{i}	3.262 (9)	Nb—Nb^{i}	3.213 (16)
Ta—Ta^{ii}	3.321 (9)	Nb—Nb^{ii}	3.398 (16)
Ta—O1^{iii}	2.07 (7)	Nb—O1^{iii}	2.05 (8)
Ta—O1^{iv}	2.22 (8)	Nb—O1^{iv}	2.09 (8)
Ta—O1^{v}	2.13 (7)	Nb—O1^{v}	2.18 (8)
Ta—O2^{vi}	1.71 (7)	Nb—O2^{vi}	1.74 (8)
Ta—O2^{vii}	2.06 (8)	Nb—O2^{vii}	2.02 (8)
Ta—O3	2.22 (4)	Nb—O3	2.27 (4)
Ta—O3^{vii}	2.18 (6)	Nb—O3^{vii}	2.16 (6)
O1—O1^{viii}	2.33 (11)	O1—O1^{viii}	2.03 (12)
O1—O1^{ix}	2.49 (10)	O1—O1^{ix}	2.56 (11)
O1—O2^{x}	2.86 (10)	O1—O2^{x}	2.83 (11)
O1—O2^{xi}	2.57 (10)	O1—O2^{xi}	2.55 (11)
O1—O2^{v}	2.17 (11)	O1—O2^{v}	2.29 (11)
O1—O2^{iv}	2.99 (10)	O1—O2^{iv}	2.82 (11)
O1—O3	2.43 (7)	O1—O3	2.46 (8)
O2—O2^{iv}	2.53 (10)	O2—O2^{iv}	2.66 (11)
O2—O3^{xii}	2.75 (11)	O2—O3^{xii}	2.89 (11)
O2—O3^{xiii}	2.07 (8)	O2—O3^{xiii}	2.16 (8)
O2—O3^{iv}	2.53 (11)	O2—O3^{iv}	2.52 (11)

Symmetry codes: (i) $-x, y, -z$; (ii) $1-x, y, 1-z$; (iii) $x, y, -1+z$; (iv) $-x, y, 1-z$; (v) $\frac{1}{2}-x, -\frac{1}{2}+y, 1-z$; (vi) $x, -1+y, z$; (vii) $\frac{1}{2}+x, -\frac{1}{2}+y, z$; (viii) $-x, y, 2-z$; (ix) $\frac{1}{2}-x, -\frac{1}{2}+y, 2-z$; (x) $-x, -1+y, 1-z$; (xi) $\frac{1}{2}+x, -\frac{1}{2}+y, 1+z$; (xii) $x, 1+y, z$; (xiii) $\frac{1}{2}+x, \frac{1}{2}+y, z$.

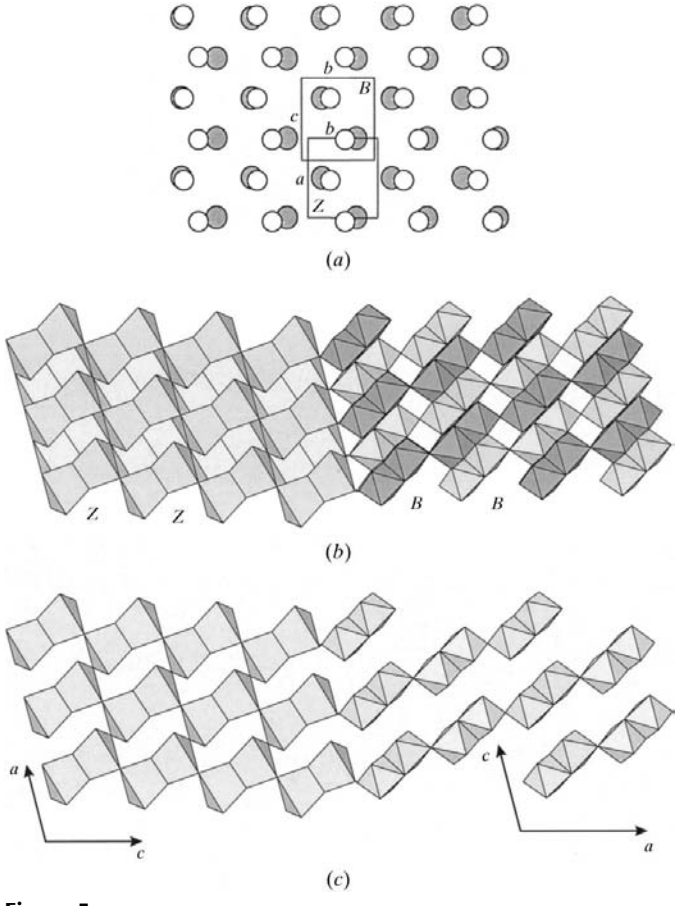

Figure 5
The common oxygen plane between the *Z*-Ta_2O_5 and *B*-Ta_2O_5 structures is illustrated in (*a*). The idealized structure model shows the intergrowth of *Z*-Ta_2O_5 (left) and *B*-Ta_2O_5 (right) ([010] zone). A possible connection between the two structures (*b*) within one layer perpendicular to the *b* axis is illustrated in (*c*).

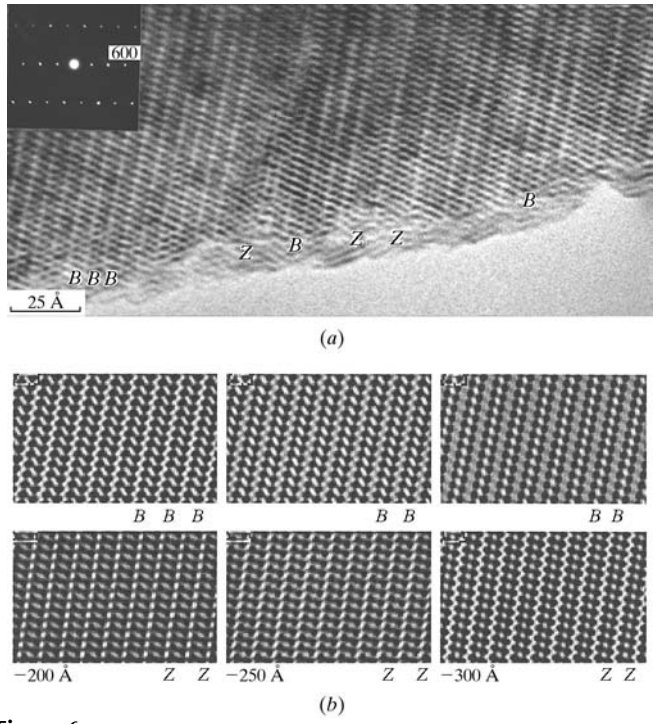

Figure 6
HRTEM image of the *B*-Ta_2O_5 ([010] zone) with the corresponding electron-diffraction pattern inserted is shown in (*a*). The rutile-like slabs are marked *B* and the defect slabs are marked *Z*. (*b*) A set of simulated images of *B*-Ta_2O_5 (top) and *Z*-Ta_2O_5 (bottom); crystal thickness $\simeq$ 30 Å, defocus values = −200, −250 and −300 Å.

transforms reversibly to B-Ta_2O_5 when the pressure is released. The HRTEM study also showed both ordered and disordered B-Ta_2O_5 crystals, indicating a reversible transformation between the two high-pressure modifications. Reversible transformations between B and Z have previously been observed for the analogous Nb_2O_5 polymorphs (Zibrov *et al.*, 1998). The results obtained also show that B-Ta_2O_5 is a stable high-pressure modification of Ta_2O_5. Further investigation of the P–T phase diagram of Ta_2O_5 is under way.

7. Discussion

The structural study indicates that B-Ta_2O_5 and Z-Ta_2O_5 coexist at the atomic level. The latter phase, which is more dense, seems to form domains within the B-Ta_2O_5 structure. This is in agreement with previous observations made on the isostructural high-pressure phases of Nb_2O_5 (Zibrov *et al.*, 1998). It should also be mentioned that intergrowth of two high-pressure phases at the atomic level has previously been observed within other structure types. W_3O_8, for example, forms two high-pressure phases of the same stoichiometry, W_3O_8(I) and W_3O_8(II). The structure of W_3O_8(I), which is more dense, was observed to form domains within the W_3O_8(II) regions (Sundberg *et al.*, 1993). It is interesting to note that the oxygen arrangements parallel to (010) in Z-Ta_2O_5 and Z-Nb_2O_5 are almost identical and very similar to a part of that in W_3O_8(I).

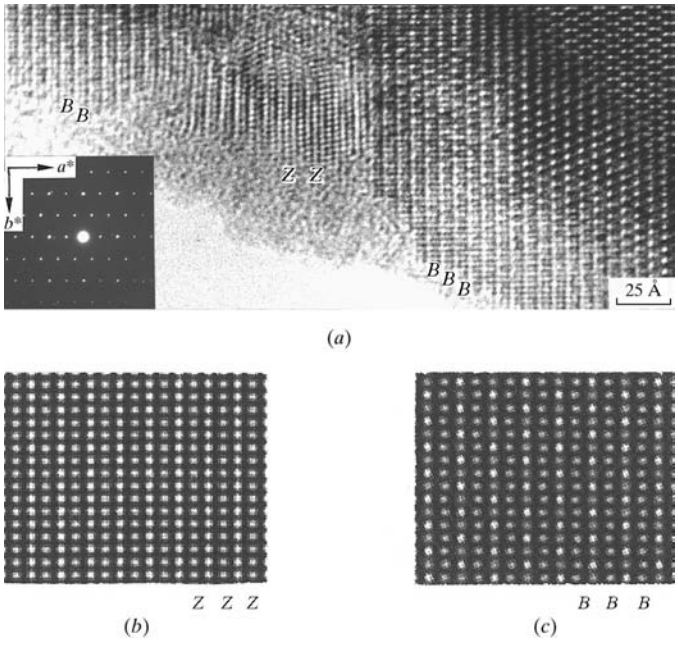

Figure 7
HRTEM image of B-Ta_2O_5 ([001] zone) with the corresponding electron-diffraction pattern inserted is shown in (*a*). A defect region of Z-Ta_2O_5 can be seen in the middle of the micrograph. (*b*) Simulated image of Z-Ta_2O_5; defocus value −200 Å, crystal thickness ∼30 Å. (*c*) Simulated image of B-Ta_2O_5; defocus value −200 Å, crystal thickness ∼30 Å.

L-Ta_2O_5 and T-Nb_2O_5 are known to have closely related structures based on the same UO_3-type subcell units. This means that a similar relationship between the Z-Ta_2O_5 and L-Ta_2O_5 structures can be found, as was recently shown for the Z-Nb_2O_5 and T-Nb_2O_5 structures (Zibrov *et al.*, 1998). The L-Ta_2O_5 structure is built up of TaO_6 octahedra and pentagonal TaO_7 bipyramids, while Z-Ta_2O_5 is only composed of seven-coordinated Ta atoms in TaO_7 polyhedra of unusual shape. However, a similar type of seven-coordination as that observed in Z-Ta_2O_5 has been found in the mineral baddeleyite, ZrO_2 (McCullough & Trueblood, 1959), and in $Nb_2Zr_6O_{17}$ (Galy & Roth, 1973).

It should also be mentioned that the diffraction peaks characteristic of B-Ta_2O_5 are very broad, approximately twice as broad as those from the Z-Ta_2O_5 modification. Similar observations were made on the Nb_2O_5 polymorphs (Zibrov *et al.*, 1998). The reason for this phenomenon is still not clear. However, the broad peaks might reflect the transformation state from Z-Ta_2O_5 to B-Ta_2O_5 and the faults and intergrowth structures observed in the B-Ta_2O_5 crystals. This will be the subject of forthcoming studies.

The authors thank Dr Bengt-Olov Marinder for his kind interest in this work and for stimulating discussions. The research described here was partly made possible by a Visiting Scientist grant from the Royal Swedish Academy of Sciences through its Nobel Institute for Chemistry. This support is gratefully acknowledged. This study forms part of a research project financially supported by the Swedish Natural Science Research Council.

References

Bérar, J. F. & Lelann, P. (1991). *J. Appl. Cryst.* **24**, 1–5.
Ercit, T. S. (1991). *Miner. Petrol.* **43**, 217–223.
Galy, J. & Roth, R. S. (1973). *J. Solid State Chem.* **7**, 277–285.
Hill, R. J. & Flack, H. D. (1987). *J. Appl. Cryst.* **20**, 356–361.
Hummel, H.-U., Fackler, R. & Remmert, P. (1992). *Chem. Ber.* **25**, 551–556.
Izumi, F. & Kodama, H. (1979). *J. Less-Common Met.* **63**, 305–307.
Johansson, K.-E., Palm, T. & Werner, P.-E. (1980). *J. Phys. E*, **13**, 1289–1291.
Lagergren, S. & Magnéli, A. (1952). *Acta Chem. Scand.* **6**, 444–446.
McCullough, J. D. & Trueblood, K. N. (1959). *Acta Cryst.* **12**, 507–511.
O'Keefe, M. A., Buseck, P. R. & Iijima, S. (1978). *Nature*, **274**, 322–324.
Shannon, R. D. & Prewitt, C. T. (1969). *Acta Cryst.* B**25**, 925–945.
Stephenson, N. C. & Roth, R. S. (1971*a*). *Acta Cryst.* B**27**, 1037–1044.
Stephenson, N. C. & Roth, R. S. (1971*b*). *J. Solid State Chem.* **3**, 145–153.
Sundberg, M., Zakharov, N. D., Zibrov, I. P., Barabanenkov, Yu. A., Filonenko, V. P. & Werner, P. (1993). *Acta Cryst.* B**49**, 951–958.
Wiles, D. B., Sakthivel, A. & Young, R. A. (1988). *DBW*3.2*S User's Guide*, Version 8804. School of Physics, Georgia Institute of Technology, Atlanta, USA.
Zibrov, I. P., Filonenko, V. P., Werner, P.-E., Marinder, B.-O. & Sundberg, M. (1998). *J. Solid State Chem.* **141**, 205–211.